JBC RESEARCH ARTICLE

Sequence- and structure-guided improvement of the catalytic performance of a GH11 family xylanase from *Bacillus subtilis*

Received for publication, July 28, 2021, and in revised form, September 25, 2021 Published, Papers in Press, October 1, 2021,
https://doi.org/10.1016/j.jbc.2021.101262

Lijuan Wang[1], **Kun Cao**[1], **Marcelo Monteiro Pedroso**[2], **Bin Wu**[1,*], **Zhen Gao**[1,*], **Bingfang He**[1], **and Gerhard Schenk**[2]
From the [1]*College of Biotechnology and Pharmaceutical Engineering, Nanjing Tech University, Jiangsu, China;* [2]*School of Chemistry and Molecular Biosciences, The University of Queensland, St. Lucia, Brisbane, Queensland, Australia*

Edited by Gerald Hart

Xylanases produce xylooligosaccharides from xylan and have thus attracted increasing attention for their usefulness in industrial applications. Previously, we demonstrated that the GH11 xylanase XynLC9 from *Bacillus subtilis* formed xylobiose and xylotriose as the major products with negligible production of xylose when digesting corncob-extracted xylan. Here, we aimed to improve the catalytic performance of XynLC9 *via* protein engineering. Based on the sequence and structural comparisons of XynLC9 with the xylanases Xyn2 from *Trichoderma reesei* and Xyn11A from *Thermobifida fusca*, we identified the N-terminal residues 5-YWQN-8 in XynLC9 as engineering hotspots and subjected this sequence to site saturation and iterative mutagenesis. The mutants W6F/Q7H and N8Y possessed a 2.6- and 1.8-fold higher catalytic activity than XynLC9, respectively, and both mutants were also more thermostable. Kinetic measurements suggested that W6F/Q7H and N8Y had lower substrate affinity, but a higher turnover rate (k_{cat}), which resulted in increased catalytic efficiency than WT XynLC9. Furthermore, the W6F/Q7H mutant displayed a 160% increase in the yield of xylooligosaccharides from corncob-extracted xylan. Molecular dynamics simulations revealed that the W6F/Q7H and N8Y mutations led to an enlarged volume and surface area of the active site cleft, which provided more space for substrate entry and product release and thus accelerated the catalytic activity of the enzyme. The molecular evolution approach adopted in this study provides the design of a library of sequences that captures functional diversity in a limited number of protein variants.

Endo-β-1,4-xylanase (EC. 3.2.1.8) randomly cleaves the β-D-xylopyranose bond between two D-xylopyranosyl residues linked by β-(1,4) bond and is a crucial enzyme in xylan degradation (1). To date, xylanases have been successfully used in a wide range of industrial applications, including pulp bleaching, animal feed manufacture, food preparation, and biofuel production (2). Accordingly, a crucial application of xylanases, supported by their high specificity and limited impact on the environment, is in the production of emerging prebiotics xylooligosaccharides (XOS) from various agro-industrial wastes (3). Among the nondigestible oligosaccharides, XOS exhibit higher resistance to acidic pH and heat and a better ability to stimulate the growth of *Bifidobacterium*. In addition, XOS have also been shown to improve calcium absorption, bowel function, and lipid metabolism and were also reported to offer protection against cardiovascular disease and reduce the risk to develop colon cancer (4). However, the major current limitations for the wide applications of XOS are high production costs and low yields (4, 5).

Numerous xylanases from bacteria, fungi, and yeasts have been isolated, purified, and characterized to date (6). Based on the sequence homologies and hydrophobic cluster analyses, most of the xylanases belong to glycoside hydrolase (GH) families 10 and 11, while a smaller number belongs to families 5, 8, and 30. GH10 xylanases typically have a high molecular mass and feature a (β/α)8-barrel fold, while GH11 xylanases display a conserved β-jelly roll fold (7). In contrast to their counterparts from the GH10 family, GH11 xylanases are regarded as "true xylanases" and are attractive because of their small size, strict substrate specificity, and a range of optimal pH values and temperatures (7, 8). Although numerous GH11 xylanases have been mined and characterized with a view to meet various industrial demands, most of these naturally occurring GH11 xylanases are unsuitable for industrial applications because of their poor specific activities and biochemical properties (9, 10). Therefore, the engineering of GH11 xylanases by directed evolution and rational design is gaining increasing attention. Rational design *via* site-directed mutagenesis or peptide segment substitution has already been successfully used to enhance the catalytic activity of several GH11 xylanases. For instance, a study using virtual mutations and molecular dynamics (MD) simulations of the GH11 xylanase AnXynB from *Aspergillus niger* indicated that the amino acid residues at the −3 subsite played a crucial role in substrate binding, and specific mutations in this site (in particular, the S41N/T43E double mutant) increased the catalytic activity by 1.7-fold (11). A similar study showed that the double mutant W125F/F163W of XynCDBFV from *Neocallimastix patriciarum* had a 20% increase in the catalytic activity compared with the WT enzyme (12). Although some

* For correspondence: Bin Wu, wubin1977@njtech.edu.cn; Zhen Gao, gaozhen_njtech@163.com.

impressive results have been achieved, learning how to construct a "small but smart" library to develop better xylanases for XOS production by utilizing the natural diversity of xylanase sequences and structures has remained challenging.

XOS with a low degree of polymerization, such as xylobiose (X2) and xylotriose (X3), present a higher prebiotic activity, while xylose (X1) itself is an undesirable component that needs to be removed (4). Therefore, xylanases that are able to produce high levels of XOS with a low degree of polymerization, while minimizing the occurrence of xylose, have great application value (13). Currently, commercially useful xylanases are mainly obtained from *Bacillus* species. Thus, enhancing the catalytic efficiency of a xylanase from *Bacillus* species is undoubtedly of great significance to the biotechnology sector as this will decrease enzyme costs and broaden its scope of application. In a previous study, we cloned and expressed the GH11 xylanase XynLC9 from *Bacillus subtilis*. The recombinant enzyme exhibited effective alkaline pH tolerance and specific hydrolysis characteristics, which mainly liberated X2 and X3 from corncob-extracted xylan, but only negligible amounts of X1 (14). Accordingly, XynLC9 is an attractive candidate for commercial utilization and thus appropriate as a starting point for further exploration and development. In the present study, we aimed to improve the catalytic performance of XynLC9. Our strategy was guided by a detailed structural comparison between XynLC9 and two well-known GH11 xylanases, xyn2 from *Trichoderma reesei* and Xyn11A from *Thermobifida fusca*, both of which had higher catalytic activity than XynLC9. Residues 5-YWQN-8 in XynLC9 were then selected as focal points for protein engineering using saturation and iterative mutagenesis. Experimental work was accompanied by MD simulations to rationalize the observed improvements of the activity among the engineered mutants of XynLC9. The present findings significantly advance the understanding of structure–function relationships in GH11 xylanases, which may thus also be applicable for the rational design of other GH11 xylanases.

Results

Selection of mutation sites based on the structural alignments of GH11 xylanases

Protein structure alignments provide an excellent tool to identify amino acid side chains and/or structural regions and patches that play an instrumental role in the function and mechanism of enzymes (11). We first established the model structure of XynLC9 using *B. subtilis* 168 xylanase BsXynA (1XXN) as the template. As shown in Fig. S1, XynLC9 displayed an overall β-jelly roll structure typical of GH11 xylanases, resembling the shape of a partially closed right hand and comprised two twisted β-sheets (named A and B) and a single α-helix. The β-sheet A was composed of five antiparallel β-strands (A2–A6), and β-sheet B contained eight β-strands (B2-B9). Both β-strands A and B constituted the "fingers", and a twisted pair of β-strands B together with α-helix formed the "palm." The large cleft between the "finger" and the "palm" domains was regarded as the active site, with two catalytic glutamate residues (Glu78 and Glu172) residing on B6 and B4. A loop between β-strands B7 and B8 created the "thumb" domain, which was critical for controlling substrate access to the active site, while another loop between the B6 and B9 strands formed a "cord" that connected the "fingers" with the base of the "thumb" (15).

The structural model of XynLC9 was used to identify functionally relevant residues and regions by comparing it with the structures of related GH11 xylanases that had superior catalytic activity and whose primary reaction products were X2 and/or X3. Suitable candidates are xyn2 from *T. reesei* and Xyn11A from *T. fusca* with specific activity of 1080 U/mg and 960 U/mg (16, 17), respectively, which is approximately 1.8- and 1.6-fold higher than that of XynLC9. Furthermore, the main products formed by xyn2 and Xyn11A were X3 and X2, respectively (16, 18). A multiple sequence alignment illustrated that XynLC9 shared 47% and 62% sequence identity with xyn2 and Xyn11A, respectively (Fig. 1*A*). Structural superimposition revealed that XynLC9 shared similar structure to xyn2 and Xyn11A with RMSD values of 1.86 Å and 2.09 Å, respectively, demonstrating that structures were better conserved than sequences. Moreover, three xylanase–xylohexaose complexes were aligned to assess the structural conservation of the active site regions. In contrast to xylanases xyn2 and Xyn11A, XynLC9 lacked the N-terminal β-strand B1 region; thus, XynLC9 only possessed five subsites that were categorized as +1, +2, and +3, toward the reducing (aglycone) end, and −1 and −2, toward the nonreducing (glycone) end, where subsite −3 was missing. Moreover, our results indicated that the structures of three enzymes in the active site were more conserved because the superimposition of three specific regions provided RMSD values of 1.34 Å and 0.43 Å, respectively. The significant active site variation between XynLC9 and the other two xylanases was mainly focused on the edge of glycone subsites (Fig. 1*B*) that harbored four consecutive amino acid residues 5-YWQN-8 in XynLC9 (FYSY in xyn2 and FYSF in Xyn11A). Consequently, we engineered XynLC9 with 5-YWQN-8 residues as the mutation targets.

Semirational engineering of XynLC9

In this study, a semirational approach was used to engineer the entrance region of the active site of XynLC9. One pair of spatially adjacent residues, Tyr5 and Gln7, was mutated by iterative saturation mutagenesis to capture possible synergistic conformational effects, while the other two residues (Trp6 and Asn8) were subjected to single-site saturation mutagenesis (Fig. 2*A*). Considering both screening effort and library coverage, NDT codon degeneracy was applied for the construction of Tyr5-Gln7 iterative saturation mutagenesis (19). Thus, three focused libraries were constructed: library A (W6X), library B (N8X), and library C (Y5X/Q7X). After the initial screening of the mutant libraries, only the mutant W6F in library exhibited marginal improvement in the specific activity (nearly 10% increase). In library B, the N8Y mutant displayed the highest specific activity (1087 U/mg), which was about 1.8-fold higher than that of WT XynLC9. The most

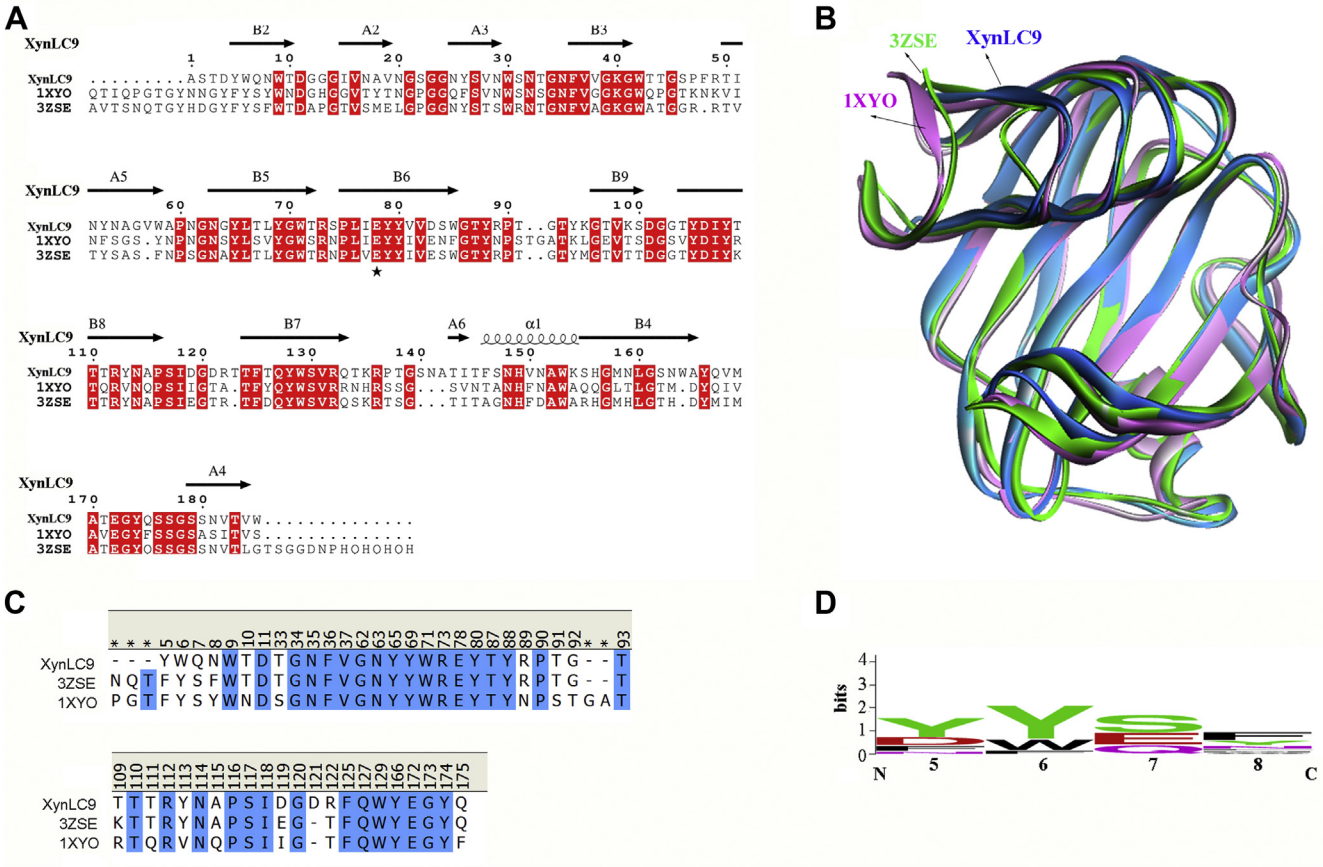

Figure 1. Sequence and structural comparisons between relevant GH11 xylanases. *A*, multiple sequence alignment of XynLC9 and two other GH11 xylanases, xyn2 from *Trichoderma reesei* (1XYO) and Xyn11A from *Thermobifida fusca* (3ZSE). Strictly conserved residues are highlighted by a *red* background. The secondary structure of XynLC9 is shown above the aligned sequences. *B*, structure alignment of XynLC9 and two GH11 xylanases (xyn2 and Xyn11A). *C*, multiple sequence alignment of the active site sequences of XynLC9 and two GH11 xylanases (xyn2 and Xyn11A). *D*, sequence logo of multiple sequence alignment of about 80 GH11 xylanases from the NCBI protein database. Conservation levels of each amino acid are indicated by the size of the letter.

efficient mutant in library C was Y5/Q7H, with about 20% increase in activity when compared with WT XynLC9 (Fig. 2*B*). Moreover, each of the three libraries contained one positive mutant, indicating that the catalytic activity of XynLC9 was vulnerable to the mutations in the N-terminal region near the active site. Site-directed mutagenesis was

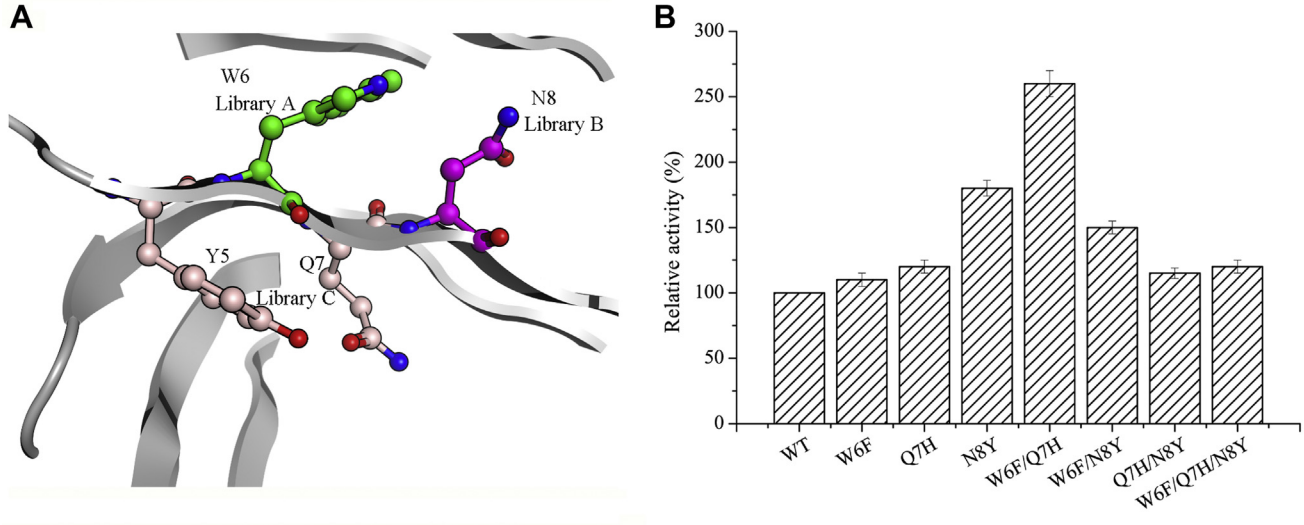

Figure 2. Mutants of XynLC9 and their catalytic activities. *A*, design of libraries for the engineering of XynLC9. *B*, comparative activity analysis of XynLC9 and its mutants with increased activity. The activity of each mutant is presented as the percentage in comparison with that of WT enzyme. The error bar represents the SDs from three replicates.

performed to probe if these mutations might have synergetic effects. We generated three double mutants (W6F/Q7H, W6F/N8Y, and Q7H/N8Y) and one triple mutant (W6F/Q7H/N8Y) (Fig. S2), followed by the assay of enzyme activity. While each of these mutants was more active than WT XynLC9, the double mutant W6F/Q7H displayed the most significant enhancement of the specific activity (260%, Fig. 2*B*). Thus, the single mutant N8Y and double mutant W6F/Q7H were selected for subsequent analyses.

Comparison between WT XynLC9 and its mutants

The enzymatic properties of mutants N8Y and W6F/Q7H were investigated using beechwood xylan as the substrate. As shown in Figure 3*A*, XynLC9 and its N8Y and W6F/Q7H mutants exhibited maximal xylanase activity at pH 7.0. Also, the three enzymes had similar pH stability, retaining more than 60% of their initial activities when incubated over 12 h at pH values ranging from 6 to 9 (Fig. 3*B*). Mutants N/8Y and W6F/Q7H had an optimum temperature of 60 °C (Fig. 3*C*), which was identical to WT XynLC9. However, two mutants showed improved thermostability, with the N8Y and W6F/Q7H mutants retaining 51.3% and 62.2% of the original activity after incubation at 50 °C for 4 h, while XynLC9 only maintained about 35.5% activity (Fig. 3*D*). Hence, as a result of their increased specific activity and thermostability, the two mutants of XynLC9 are promising candidates for industrial applications.

Hydrolysis products of XOS and beechwood xylan by XynLC9 and two variants were analyzed using the TLC method. As shown in Figure 4, none of the enzymes were active toward X2 and X3 but showed a similar product range when X4 and X5 were used as substrates. When using X4 as a substrate, XynLC9 and its mutants, N8Y and W6F/Q7H,

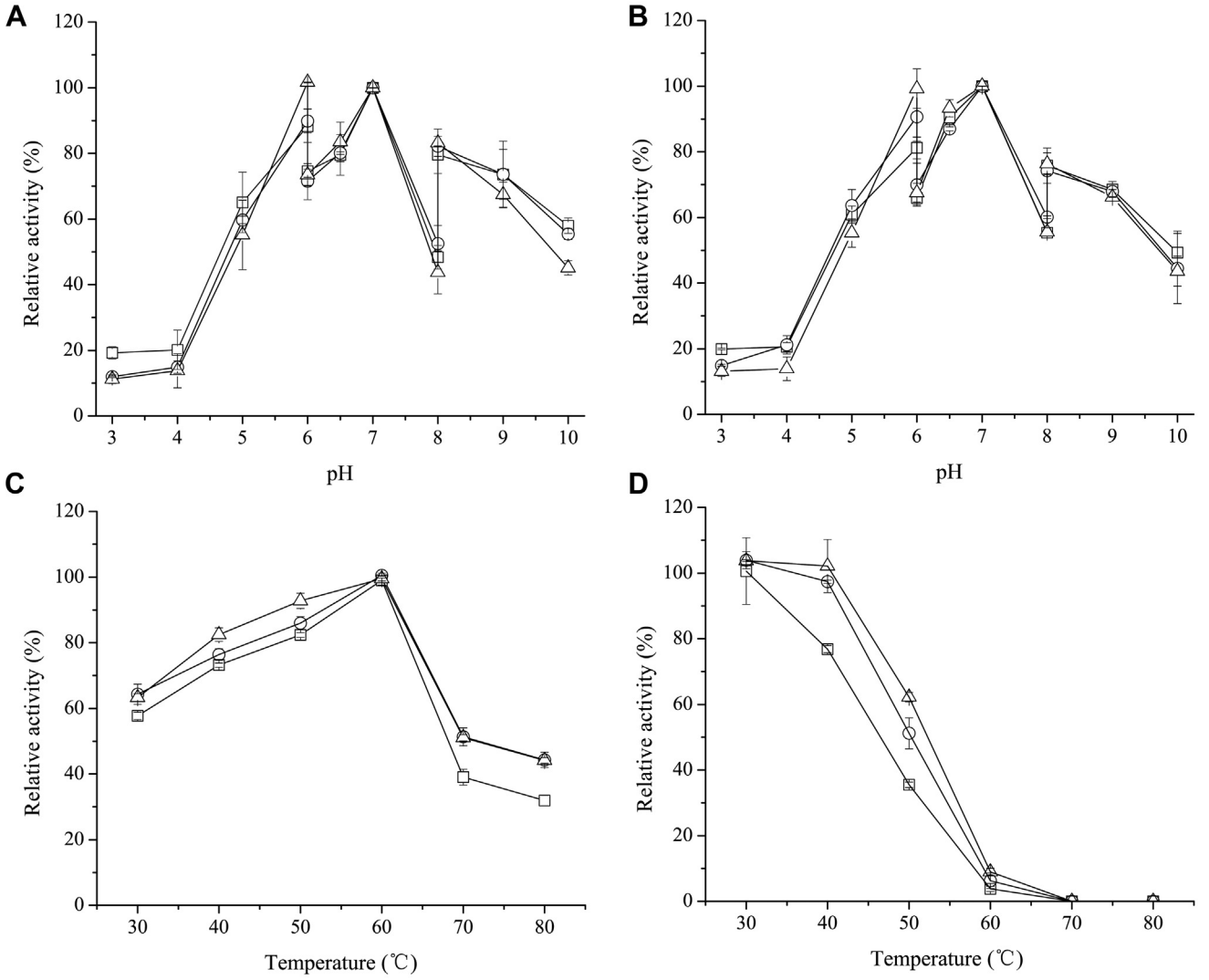

Figure 3. Effect of temperature and pH on the activity and stability of XynLC9 and its mutants. *A*, activity of XynLC9 and its mutants was measured at different pH values at 60 °C. *B*, pH stability of XynLC9 and its mutants was evaluated at 4 °C for 12 h at different pH values. *C*, the effect of temperature on activity of XynLC9 and its mutants was studied by changing the temperature from 30 to 80 °C at pH 7.0. *D*, thermostability of XynLC9 and its mutants was measured by incubating the enzyme at various temperatures for 4 h. Symbols used are as follows: XynLC9 (□), N8Y (○), and W6F/Q7H (Δ). The error bar represents the SDs from three replicates.

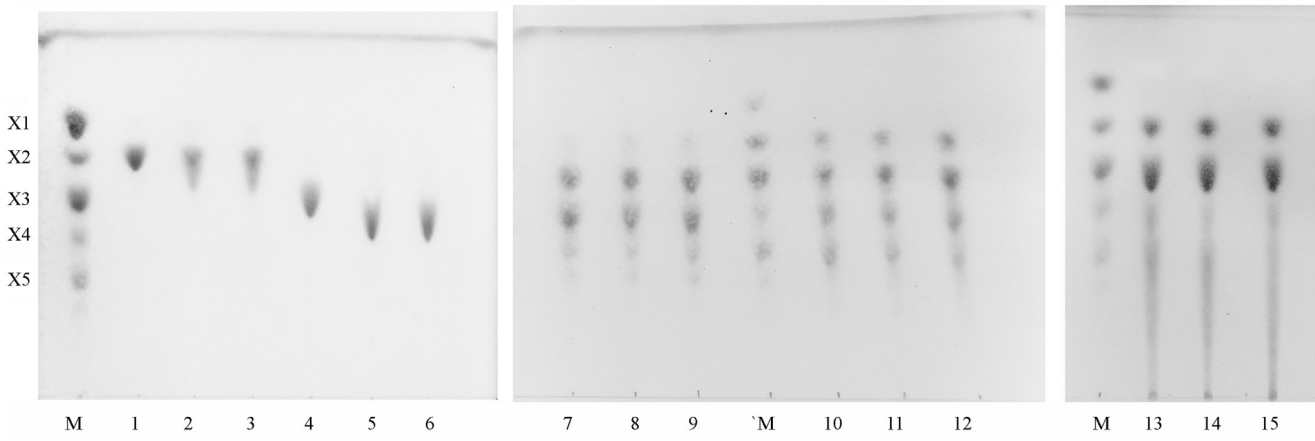

Figure 4. TLC analysis of hydrolysis products from xylooligosaccharides and beechwood xylan by XynLC9 and its mutants. Lane M, xylose unit markers, that is, xylose (X1), xylobiose (X2), xylotriose (X3), xylotetraose (X4), and xylopentaose (X5); lanes 1 to 12, products released from xylobiose (1–3), xylotriose (4–6), xylotetraose (7–9), and xylopentaose (10–12) by XynLC9, N8Y, and W6F/Q7H; lanes 13 to 15, hydrolysis products from beechwood xylan by XynLC9, N8Y, and W6F/Q7H.

displayed similar distribution with X3 as the major products. During the hydrolysis of X5, the primary products were X2 and X3, while smaller quantities of X4 and trace amounts of undigested X5 were also present in the reaction mixture. The same analysis was also performed using beechwood xylan as a substrate. Again, for each of the three enzymes, X2 and X3 were the primary products formed (Fig. 4), while the amounts of X4 and X5 in the mixture were minimal.

The apparent kinetic parameters of XynLC9 and its mutants were determined by using beechwood xylan as the substrate (Table 1). The apparent K_m values for N8Y and W6F/Q7H were higher than that for XynLC9, indicating the reduced substrate affinity (20). However, the turnover rate (k_{cat}) of two mutants was significantly higher than that of XynLC9, indicating that the mutants performed better than the WT to convert most of the bound substrate into product (21). Owing to the considerable improvement in k_{cat} values, N8Y and W6F/Q7H displayed about 22% and 47% higher catalytic efficiency (k_{cat}/K_m), respectively, than the WT, which is consistent with the enzyme activity results described above.

Structural comparisons and MD simulations of WT XynLC9 and its mutants

Structural comparisons and MD simulations were performed for WT XynLC9 and the N8Y and W6F/Q7H mutants to explore the possible molecular basis that has led to the improved catalytic efficiency of the mutants. CD spectroscopy demonstrated that the mutations in positions 6 to 8 had no measurable effect on the secondary structural elements of XynLC9 (Fig. S3). Next, MD simulations were performed over a 50-nm time scale for WT XynLC9 and two mutants. The RMSD of the α-carbon atoms of the three enzymes in the presence of the substrate reached equilibrium after 40 ns, and thus, only the MD trajectories of the last 10 ns were selected for further analysis (Fig. 5*A*). The RMSD values were slightly higher for two mutants than for WT XynLC9, suggesting that the structural ensemble generated by MD simulations differed more from the initial structure in the case of mutants N8Y and W6F/Q7H than WT XynLC9 (22). Root mean square fluctuation (RMSF) reflects the flexibility of each residue during the simulations. The analysis of RMSF values per residue did not show any significant changes at positions 5 to 8 between XynLC9 and two mutants (Fig. 5*B*). However, a slight increase in RMSF values was observed for the N8Y mutant over positions 10 to 12, indicating that the neighboring residues were more flexible with Tyr at position 8 than Asn at the same position (15). Nevertheless, this situation was reversed for the double mutant W6F/Q7H, with RMSF values smaller than that of XynLC9 in the region of residues 10 to 15. These results indicated that the mutations of N8Y and W6F/Q7H altered the local backbone structure flexibility of the enzyme, thus affecting the interactions between the enzyme and substrate.

To further probe the structural changes caused by mutations at positions 6 to 8, a superimposition of the structures of WT XynLC9 and the two mutants was performed using the average structures extracted from the final 10 ns of the equilibrated state of the MD simulations as references for the final functional forms of the proteins. In native XynLC9, residues 6 to 8 were located on the active site cleft and in β-strand B2 of the N-terminal region. The Asn to Tyr substitution at residue 8 involved a neutral charge amino acid exchange to a bulky aromatic amino acid, which facilitated the formation of a new hydrogen bond between Tyr8 and Val16. In addition, there was a hydrophobic stacking interaction between this tyrosine and Trp6 (Fig. 6). On the other hand, Trp6 of WT XynLC9 interacted with Asn8, Ala18, and Asn20 (Fig. 6). Replacement of Trp6 by phenylalanine with a relatively smaller

Table 1
Kinetic values of XynLC9 and its mutants toward beechwood xylan

Enzyme	K_m (mg/ml)	k_{cat} (/s)	k_{cat}/K_m (ml/mg/s)
XynLC9	7.2 ± 0.6	55.9 ± 4.8	7.8 ± 0.7
N8Y	11.2 ± 0.9	105.7 ± 11.2	9.5 ± 0.8
W6F/Q7H	11.6 ± 0.9	133.1 ± 11.7	11.4 ± 0.9

The error bar represents the SDs from three replicates.

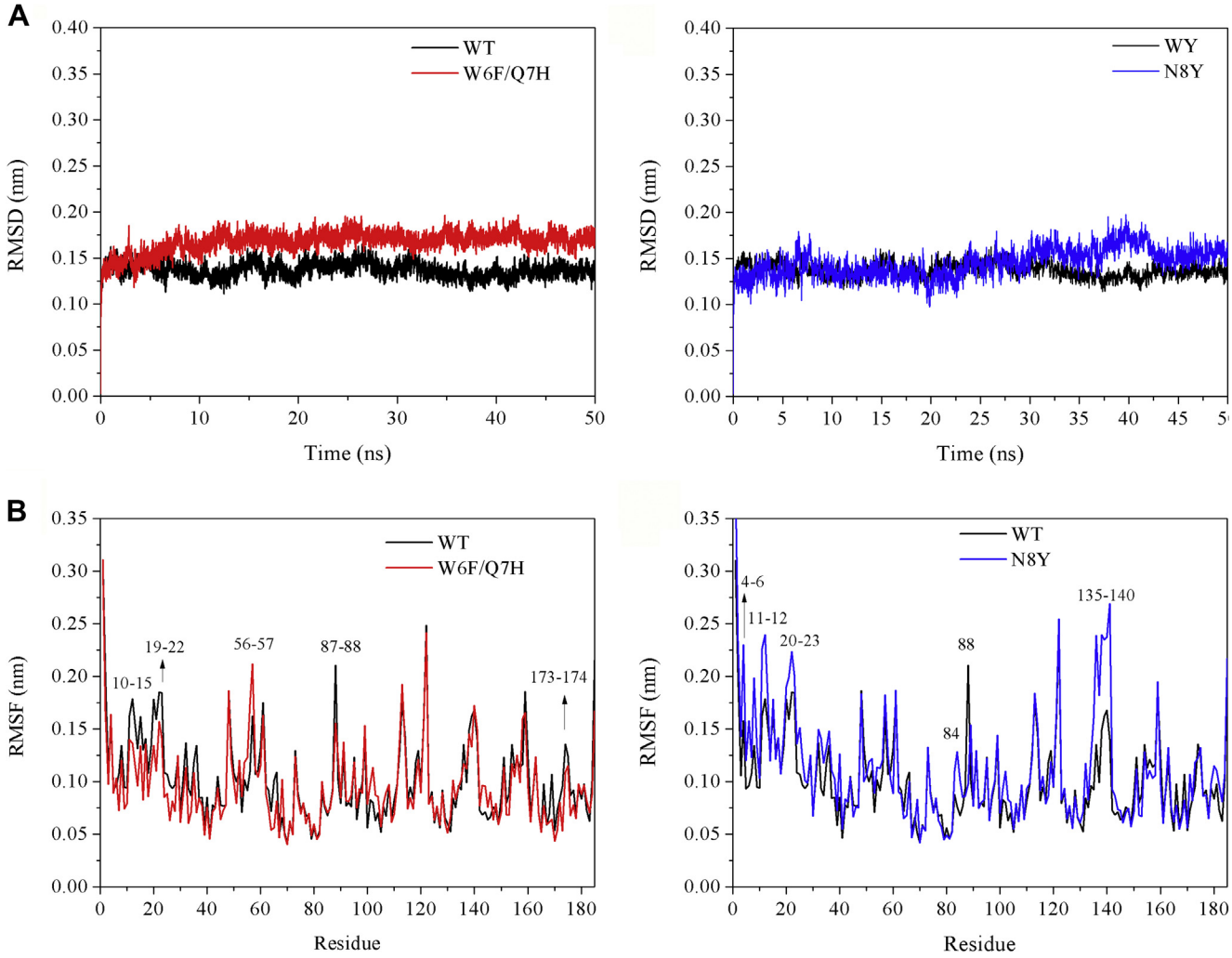

Figure 5. Molecular dynamics simulations with XynLC9. The RMSD (*A*) and RMSF (*B*) values of XynLC9 and its mutants during 50-ns molecular dynamics simulation. The trajectories of the last 10 ns were used for data analyses. RMSF, root mean square fluctuation.

side group eliminated these interactions (Fig. 6). Gln7 was oriented toward the active site cleft near the catalytic site. The major hydrogen bond interactions in β-strand B2 of His7 in the double mutant W6F/Q7H and the equivalent residue (Gln7) in WT XynLC9 were conserved. These included two intramolecular hydrogen bonds between the main-chain carbonyl oxygen of position 7 and the main-chain amide nitrogen of Gly39 and between the side chain of the residue (His or Gln) and the side chain –OH group of Tyr5 (Fig. 6).

We also analyzed the interactions between residues 6 to 8 of XynLC9 or its mutants and the substrate xylohexaose using the DS 3.5 software. The XynLC9–xylohexaose complex structure revealed that Trp6 and Asn8 might not interact directly with xylohexaose because they were distal to the substrate, while Gln7 provided two hydrogen bonds with O3 at the −2 subsite (Fig. 7). The introduction of an aromatic side chain in the N8Y mutant did not lead to the formation of CH-π stacking interactions with the substrate, but this mutation altered the conformation of Gln7 significantly, leading to the removal of one of the two hydrogen bonds between this glutamine and the −2 xylose moiety of the substrate (Fig. 7). For the W6F/Q7H double mutant, His7 only provided one hydrogen bond to the O2 of xylose residue in the −2 subsite (Fig. 7). These results indicated that mutations caused impaired binding ability to the ligand when compared with WT XynLC9.

Using the entire simulation trajectories, we calculated the surface area/volume of the active site cavity of WT XynLC9, N8Y, and W6F/Q7H to be 607 $Å^2$/879 $Å^3$, 705 $Å^2$/1004 $Å^3$, and 730 $Å^2$/1032 $Å^3$, respectively (Fig. S4 and Table 2). The introduction of the mutations led to both a greater surface area and volume, with the double mutant having the most significant effect. The larger volume and area of the active site might be conducive to the substrate entrance and product dissociation, thereby improving the catalytic activity of two mutants.

XOS production by XynLC9 and W6F/Q7H mutant from corncob-extracted xylan

To assess the potential of the engineered xylanase for XOS production, the double mutant W6F/Q7H with highest catalytic activity was selected to hydrolyze corncob-extracted

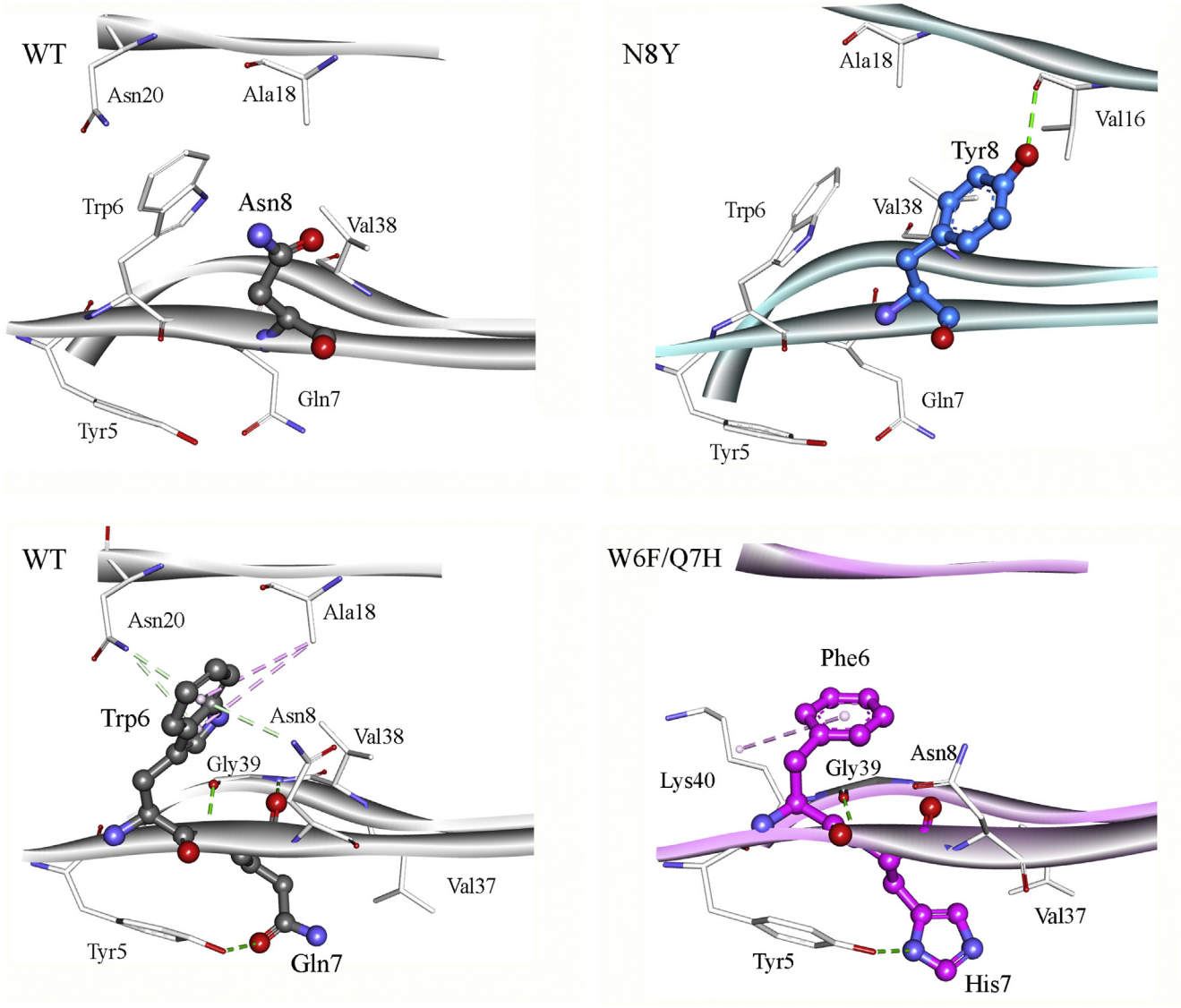

Figure 6. Effects of N8Y and W6F/Q7H mutation on the local structure of XynLC9 and their intramolecular interactions.

xylan. As shown in Figure 8, XOS production increased over time irrespective of whether corncob xylan was incubated with WT XynLC9 or mutant W6F/Q7H. However, at every time point, W6F/Q7H exhibited performance superior to that of WT XynLC9. After 14 h of incubation with the double mutant, the concentration of XOS reached 10.6 mg/ml, which was

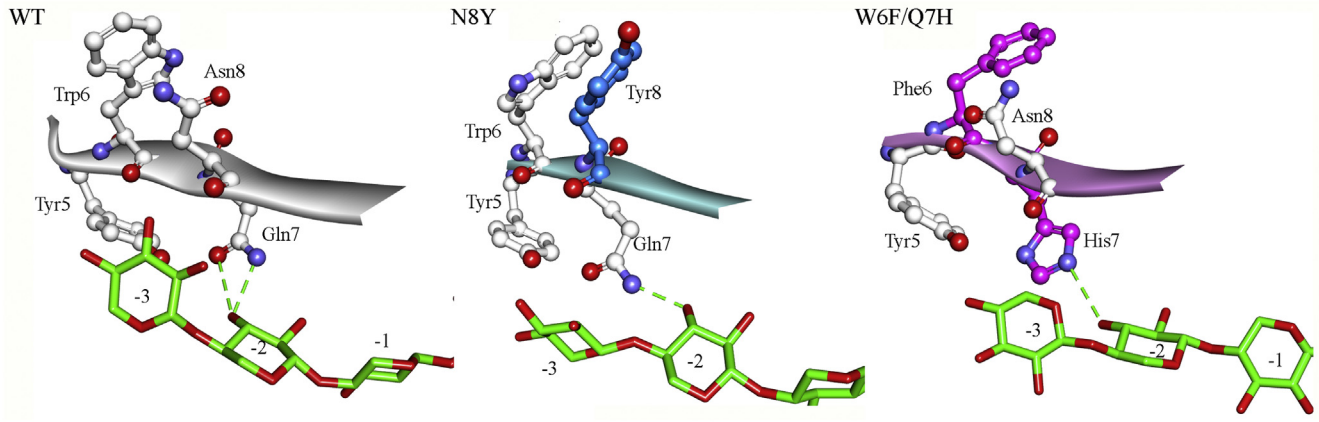

Figure 7. The hydrogen bonds formed with the complexes of XynLC9 or two mutants and xylohexaose at the region of residues from 5 to 8.

Table 2
Geometrical and topological properties of the active site of XynLC9 and its mutants

Enzyme	Volume (Å^3)	Area (Å^2)	Minimal distance (Trp9–Pro116) (Å)
XynLC9	607 ± 15	879 ± 43	10.3 ± 0.5
N8Y	705 ± 18	1004 ± 41	11.9 ± 0.8
W6F/Q7H	730 ± 12	1032 ± 37	12.1 ± 0.5

The error bar represents the SDs from three replicates.

about 1.6-fold higher yield than that of WT XynLC9. The results above indicated that the substitutions at positions 6 and 7 with Phe and His promoted the production capacity of XOS from corncob, which was consistent with the previously determined catalytic efficiency.

Discussion

Enhanced catalytic activity is one of the most desirable properties related to the xylanase engineering perspective (11, 12). Identifying suitable sites for site-directed or site-saturation mutagenesis to improve the catalytic performance of xylanases are challenging (11, 23). Therefore, structural bioinformatics is useful in exploring structure–function relationships and consequently also provide insight into protein rational design. Previously, through a structural comparison with the thermophilic xylanase XTL from *Thermomyces lanuginosus*, a double mutant of the xylanase XynA from *B. subtilis* was engineered (S22E/N32D), which had both enhanced thermostability and increased catalytic activity (24). Inspired by the previous studies, we compared the differences in the three-dimensional structure of the XynLC9 from *B. subtilis* with the xylanase xyn2 from *T. reesei* and the xylanase Xyn11A from *T. fusca* to identify the structural determinants in the xylanase XynLC9 that might be important to improve the catalytic activity of this enzyme. Multiple sequence alignment discovered that the residues lining the active site cleft were largely conserved among three xylanases (Fig. 1*C*), in agreement with the functional importance of the active site cleft. However, the four residues mentioned above were tended to be variable, 5-YWQN-8 for XynLC9 corresponded with 13-FYSY-16 for xyn2 and 14-FYSF-17 for Xyn11A. Next, we analyzed the variability of these four residues by comparing about 80 GH11 xylanases. The results indicated that the tyrosine in position 5 of XynLC9 was quite common in GH11 xylanases, but the occurrence of a tryptophan, glutamine, and aspartic acid in positions equivalent to 6, 7, and 8 in XynLC9, respectively, is rarer (Fig. 1*D*). It is well known that mutagenesis targeting those highly conserved amino acids in the active site likely leads to impaired activity. On the contrary, variable residues in the active site are normally related to the functional diversity of the homologous enzymes (11, 25). Thus, we constructed three libraries based on the spatial distance of four residues. Screening showed that, in library C (positions 5 and 7), no improved xylanase activity was observed for mutant Y5X, which was consistent with tyrosine being the most common residue in this position. However, we obtained two beneficial mutants, N8Y and W6F/Q7H, which exhibited 1.8-fold and 2.6-fold higher catalytic activity than WT XynLC9, respectively. Moreover, the 2.6-fold enhancement in the catalytic activity of XynLC9 is greater than or comparable with previous studies for engineering of GH11 xylanases conducted with site-directed mutagenesis or functional region replacement. For instance, the Y7L mutation in *Aspergillus fumigatus* xylanase RT-1 led to 1.5-fold increase in activity (26). The substitutions of Ser41 and Thr43 at −3 subsite with Asn and Glu enhanced the catalytic activity of *A. niger* xylanase XynB by 1.7-fold (11). Similar phenomena were also observed for the double mutant W125F/F163W of XynCDBFV from *Neocallimastix patriciarum*, which displayed nearly 20% increase in catalytic activity when compared with the WT (12). The catalytic activity of *B. subtilis* xylanase BsXynA was improved by 1.2-fold through introducing two Ser residues and a disulfide bridge on the "cord" region (27). Li *et al.* (13) reported that the combination of N-terminal region replacement and site-directed mutagenesis in the cord of xylanase Srxyn from *Streptomyces rochei* led to 5.3-fold increase in specific activity. In addition, all the mutated residues in our study were located in β-strand B2. Li *et al.* (28) also improved the catalytic efficiency of *Aspergillus oryzae* xylanase AoXyn11A by 1.8-fold through substituting Gly11 in β-strand B2 with Ile. However, although the β-strand B2 locates the N terminus of GH11 xylanases and forms part of the active site cleft (11), the reports about engineering GH11 xylanases in the β-strand B2 to improve the catalytic activity are limited.

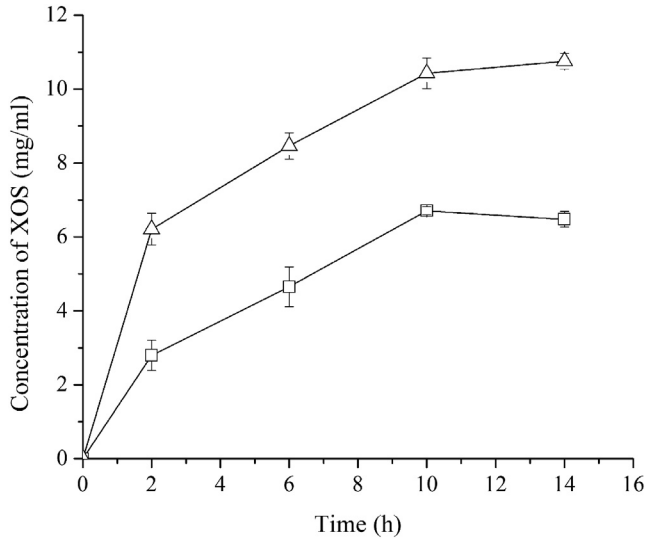

Figure 8. Time course of XOS production by XynLC9 (□) and W6F/Q7H (Δ) from corncob-extracted xylan after 14 h of incubation. The error bar represents the SDs from three replicates. XOS, xylooligosaccharides.

Both the N8Y single and W6F/Q7H double mutants of XynLC9 were selected for detailed characterization because of their significant enhancements in specific activity. Interestingly, both mutants also displayed enhanced thermostability. Usually, there is a trade-off between enzyme activity and thermostability at the level of individual mutations as enzyme rigidity is required for greater thermostability, while structural flexibility benefits high catalytic activity. Therefore, mutants with increased catalytic activity often have lower

thermostability (29, 30). However, our observations of increased catalytic activity and thermostability for the two XynLC9 mutants are not without precedence; for example, the S22E/N32D double mutant of *B. subtilis* xylanase XynA also demonstrated a 1.9-fold increase in activity and a significant improvement in thermal stability (24).

The kinetic parameters in combination with MD analyses provided insight into the improved catalytic performance of the mutants generated in this study. In comparison with WT XynLC9, both mutants had larger K_m values for xylan, indicating impaired substrate-binding affinity. In agreement with these data, molecular mechanics-poisson bolzmann surface area calculations showed that the free binding energy for the protein–ligand interaction of the mutants was higher than that of XynLC9 (−9.6 kcal/mol and −9.3 kcal/mol for N8Y and W6F/Q7H, *versus* −9.9 kcal/mol for XynLC9, respectively). However, both mutants had significantly higher k_{cat} values, suggesting that these mutations facilitated faster product release from the active site. Moreover, the degree of increase for k_{cat} values was higher than that for K_m values, resulting in improved catalytic efficiency (k_{cat}/K_m) for two mutants, which was in agreement with the improved catalytic activity of two mutants. These phenomena were similar to the results of Li *et al.* and Damis *et al.* (5, 26). The MD simulations were consistent with the experimental kinetics. Owing to the lack of β-strand B1, XynLC9 only possessed five subsites from −2 to +3; therefore, the xylose moiety at −3 subsite had no obvious interaction with XynLC9. In the XynLC9–X6 complex, Trp6 and Asn8 had no direct interaction with the substrate, while Gln7 formed two hydrogen bonds with the xylose unit at the −2 subsite. In W6F/Q7H double mutant, the phenylalanine substitution at residue 6 removed the hydrophobic interactions between W6 and residues N8, A18, and N20, resulting in a moderate expansion of the active site cleft. Besides, although Q7H mutation maintained the primary intramolecular hydrogen bond interactions, this substitution reduced hydrogen bonds between the enzyme and substrate. The calculations of the cavity surface area and volume of the active site cleft also indicated that the mutation W6F/Q7H provided a larger space for substrate entry and product release, thereby, speeding up the substrate conversion as shown by the higher k_{cat} value. The N8Y mutation led to the formation of a new hydrogen bond between Tyr8 and Val16, as well as a stacking interaction between Tyr8 and Trp6, which caused the swing of β-strand B2 toward the lateral margins of the active site, thus increasing the volume of the active site cleft. This feature was further confirmed by calculating the cavity surface area and volume of the active site cleft of mutant N8Y. In addition, for GH11 xylanases, the narrowest zone of the active site cleft is located between the conserved Pro residue of the "thumb" and the conserved aromatic residue (Trp or Tyr) of β-strand B2 (11). To compare the open state of the active site in XynLC9 and two mutants, the minimal distance between Trp9 and Pro116 was calculated on each entire simulation trajectory. The results indicated that the active site cleft in two mutants was more open than in the WT enzyme (about 12 Å *versus* about 10 Å for the minimal Trp9–Pro116 distances, Table 2). The larger opening state of the active site cleft in two mutants was also likely to contribute to their higher catalytic efficiency. Collectively, the mutations of W6F/Q7H and N8Y provided a larger space and opening state for the active site, as well as altered the interactions between the substrate and enzyme, which explained the underlying higher kinetic rate and catalytic activity of two mutants. A similar observation was also reported for the engineering of a GH11 xylanase XynCDBFV from *N. patriciarum*, where the substitution of C-terminal residues 207-NGGA-210 by 207-SSGS-210 increased the opening state of the active site cleft to facilitate substrate access to the catalytic residues, with a concomitant improvement of the catalytic efficiency (by 1.6-fold) (31). Similarly, by comparing the structural and dynamic properties of two distinct contrasting GH11 xylanases, Vucinic *et al.* (32) also reported that a larger and more extended catalytic cleft played a major role in regulating the activity of GH11 xylanases by facilitating substrate access and product release. In addition, substrate selectivity features the binding affinity of a xylanase for a given substrate, which plays an important role in several biotechnological cereal-based processes such as bread making (33). To expand the potential applications of N8Y and W6F/Q7H, the effects of these mutations on substrate selectivity will be investigated in future studies.

In enzyme engineering, learning how to establish a "small but smart" library remains a long-standing problem. In this study, based on sequence homology and structure alignments, nonconversed N-terminal residues 5-YWQN-8 in the GH11 xylanase XynLC9 from *B. subtilis* were identified as the hotspots for activity engineering of this enzyme. Two mutants, W6F/Q7H and N8Y, with enhanced catalytic activity and better thermostability were obtained by site-saturation mutagenesis and iterative mutagenesis, rendering them as valuable candidates for efficient bioconversion of polymeric substrates and production of functional oligosaccharides. Structural analysis and MD simulations provided an in-depth insight into the determinants that contributed to the improvement of the catalytic performance of two mutants. This work confirmed that the use of the natural diversity of protein sequences and structures is an effective approach to guide rational design experiments.

Experimental procedures

Structural bioinformatics analysis of the xylanase XynLC9

The amino acid sequences of xyn2 and Xyn11A were retrieved from the NCBI protein database. The three-dimensional structures of xyn2 (1XYO) and Xyn11A (3ZSE) were downloaded from the Protein Data Bank (34, 35). Multiple sequence alignments were carried out using Clustal Omega program suite. The homology model of XynLC9 was generated with the Discovery Studio (DS) 3.5 program using the crystal structure of the xylanase BsXynA (1XXN) from *B. subtilis* 168 as the template (36). The quality of final model was assessed using PROCHECK and Profile-3D. The structure model of XynLC9 was superimposed to the structures of xyn2 and Xyn11A using DS 3.5 software, and then the RMSD values

of α-carbon atoms among these three structures were calculated. For the docking analysis, the enzyme–substrate complex was constructed by docking xylohexaose molecule from *Tr*Xyn11A (4HK8) into the active site cleft of the selected xylanase using DS 3.5 software (37). Amino acid residues in the active site of three xylanases were identified using CavityPlus (http://www.pkumdl.cn:8000/cavityplus/computation.php).

Library construction and screening

Site-saturation mutagenesis libraries were constructed at sites A (Trp6) and B (Asn8) by overlap extension PCR using the plasmid pET-28a(+)/XynLC9 as the template (*Nco*I-*Xho*I restriction sites). Primer pairs are listed in Table S1. Iterative saturation mutagenesis library was performed at site C (Tyr5/Gln7) with the same template and PCR-based method. The sequences of primers are also listed in Table S1. Every engineered XynLC9 mutant was fused to a hexa-histidine tag at the C terminus to facilitate purification *via* affinity chromatography. The mutations were confirmed by DNA sequencing, and the plasmid was transformed into *Escherichia coli* BL21 (DE3) for recombinant expression using 0.1 mmol/l IPTG. Subsequently, the cells were harvested, resuspended in the lysis buffer (50 mmol/l Na_2PO_4/NaH_2PO_4, pH 7.0), and disrupted by sonication. The resulting supernatant was assayed for enzyme activity. Mutants with higher enzyme activity than WT XynLC9 were selected. Then, these mutants and XynLC9 were purified in a single step using a HisTrap FF column according to the manufacturer's recommendations. The apparent molecular weight and homogeneity of the purified enzymes were determined on a 12% SDS-PAGE gel. The concentration of the purified proteins was measured using the Bradford method (38), and the activity of the purified enzymes was measured. The specific activity (U/mg) of the mutants was calculated and compared with that of WT XynLC9.

Enzymatic activity assay

Xylanase activity of the XynLC9 and its mutants was determined using the 3,5-dinitrosalicylic acid method as described previously (14). The reaction mixture, consisting of 1 ml of 1% (w/v) beechwood xylan and 0.5 ml of a suitably diluted enzyme solution, was incubated at pH 7.0 and 60 °C for 10 min. One unit (U) of xylanase activity was defined as the amount of enzyme releasing 1 μmol of reducing sugar equivalent from xylose per minute.

Biochemical characterization of XynLC9 mutants

The optimal pH for WT XynLC9 and its mutants was determined at 60 °C with a pH range from 3 to 10 using citric acid/sodium citrate buffer (pH 3.0–6.0), sodium phosphate buffer (pH 6.0–8.0), and Tris-HCl buffer (pH 8.0–10.0). The effect of temperature on xylanase activity was determined in sodium phosphate buffer (pH 7.0) from 30 to 80 °C. To evaluate the pH stability of the enzyme, WT XynLC9 and its mutants were incubated in the abovementioned buffers at various pH values at 4 °C for 12 h. The thermostability of XynLC9 mutants was monitored by measuring residual activities after preincubation of the enzyme at different temperatures at pH 7.0 for 4 h.

The apparent kinetic parameters, that is, Michaelis constant (K_m), turnover rate (k_{cat}), and catalytic efficiency (k_{cat}/K_m) for WT XynLC9 and its mutants, were determined at 60 °C and pH 7.0 using 1 to 20 mg/ml of beechwood xylan as the substrate. The kinetic constants were obtained by fitting the experimental data to the Michaelis–Menten equation.

To evaluate the hydrolysis characteristics of XynLC9 and its mutants, standard XOS (X2–X5) and beechwood xylan were used as the substrates. For the hydrolysis of XOS, reaction systems (1 ml) containing 1 mg/ml of the substrate were incubated with 5 U of the enzyme for 3 h under the same conditions used for the activity assay. For the hydrolysis of beechwood xylan, the amount of substrate and enzyme was 10 mg/ml and 10 U, respectively. Then, the hydrolytic products were analyzed by TLC with a mixture of butanol–acetic acid–water (3:2:1, v/v/v) as the solvent system. The sugars on the plates were stained with sulfuric acid–methanol (95:5, v/v), followed by heating for 10 min at 110 °C.

Analysis of CD spectra

The spectra of WT XynLC9 and its mutants (25 μg/ml, in 10 mmol/l phosphate buffer, pH 6.0) were recorded on a Chirascan spectropolarimeter (Applied Physics Company) with the wavelength of 185 nm to 270 nm using a 1-mm-pathlength cuvette and a bandwidth of 1 nm. The temperature parameter and scanning speed were set at 20 °C and 200 nm/min, respectively. The secondary structural elements of the protein were analyzed using CDNN CD deconvolution software.

Homology modeling and MD simulations

Using the WT XynLC9–xylohexaose complex as the template, the homology model of the mutant and bound xylohexaose complex was constructed by DS 3.5 software. MD simulations were performed using GROMACS 4.5.4 program with gromos54a7 force field and the SPC water model (39, 40). The protein–sugar complex was solvated in a cubic box of water, and the edge of the box was approximately 10 Å. Sodium and chloride ions were added for maintenance of system neutrality. The LINCS algorithm was used to constrain the bonds involving hydrogen atoms (15). The long-range electrostatic interactions were calculated with the particle mesh Ewald method with 1.2-nm cut-off and 1.2-nm Fourier spacing. Before MD simulations, the energy of each system was minimized using the steepest descent method with 10,000 steps. Then, 200 ps NVT and 500 ps NPT simulations were performed in turn. The temperature was set to 300 K using V-rescale thermostat with a coupling constant of 0.1 ps. Pressure was set at 1 bar using Parrinello–Rahman pressure-coupling with a coupling coefficient of 1 ps. Finally, the simulation time was 50 ns for data analyses, allowing a time step of 2 fs, and each simulation system was repeated three times to increase the reliability of the results. The RMSD and RMSF

values were calculated from the equilibrium state. Three-dimensional molecules were analyzed and visualized by DS 2018 client. The free binding energy (ΔG) of the complexes of XynLC9 or its mutants and the ligand was calculated by Prodigy web server (http://biance.science.uu.nl/prodigyl). The surface area and volume of the active site cleft in WT XynLC9 and its mutants were calculated using CavityPlus.

Preparative application of XynLC9 mutants for XOS production

Xylan extraction from corncob was carried out with 5% NaOH at room temperature for 12 h according to the method described previously (41). Enzymatic production of XOS was performed by 0.5 mg of XynLC9 or its mutant in 20 mmol/l sodium phosphate buffer (pH 7.0) in a 100 ml total volume containing 3% (w/v) of extracted xylan. The mixture was shaken at 200 rpm and 50 °C for 14 h. Aliquots were collected at regular intervals and used to determine total reducing sugar by the 3,5-dinitrosalicylic acid method.

Data availability

All data are contained within the article.

Supporting information—This article contains supporting information (15).

Acknowledgments—We thank the National Key R&D Program of China (2018YFA0902200), the National Natural Science Foundation of China (21776135), Jiangsu Agricultural Science and Technology Innovation Fund Project (CX(19)2001), Primary Research & Development Plan of Jiangsu (BE2018395), and Qinglan Project of Jiangsu Province for their financial support.

Author contributions—B. W. and Z. G. conceptualization; L. W., K. C., M. M. P., and B. W. investigation; L. W., B. W., and Z. G. writing – original draft; K. C. and B. H. methodology; B. H. and G. S. supervision; B. H. and G. S. writing – review and editing.

Conflict of interest—The authors declare that they have no conflicts of interest with the contents of this article.

Abbreviations—The abbreviations used are: DS, Discovery Studio; GH, glycoside hydrolase; RMSF, root mean square fluctuation; XOS, xylooligosaccharides.

References

1. Nakamichi, Y., Fouquet, T., Ito, S., Watanabe, M., Matsushika, A., and Inoue, H. (2019) Structural and functional characterization of a bifunctional GH30-7 xylanase B from the filamentous fungus *Talaromyces cellulolyticus*. *J. Biol. Chem.* **294**, 4065–4078
2. Juturu, V., and Wu, J. C. (2012) Microbial xylanases: Engineering, production and industrial applications. *Biotechnol. Adv.* **30**, 1219–1227
3. Karlsson, E. N., Schmitz, E., Linares-Pasten, J. A., and Adlercreutz, P. (2018) Endo-xylanases as tools for production of substituted xylooligosaccharides with probiotic properties. *Appl. Microbiol. Biotechnol.* **102**, 9081–9088
4. Amorim, C., Silverio, S. C., Prather, K. L. J., and Rodrigues, L. R. (2019) From lignocellulosic residues to market: Production and commercial potential of xylooligosaccharides. *Biotechnol. Adv.* **37**, 107397
5. Li, Q., Sun, B. G., Xiong, K., Teng, C., Xu, Y. Q., Li, L. J., and Li, X. T. (2017) Improving special hydrolysis characterization into *Talaromyces thermophilus* F1208 xylanase by engineering of N-terminal extension and site-directed mutagenesis in C-terminal. *Int. J. Biol. Macromol.* **96**, 451–458
6. Alokika, and Singh, B. (2019) Production, characteristics, and biotechnological applications of microbial xylanases. *Appl. Microbiol. Biotechnol.* **103**, 8763–8784
7. Paes, G., Berrin, J. G., and Beaugrand, J. (2012) GH11 xylanases: Structure/function/properties relationships and applications. *Biotechnol. Adv.* **30**, 564–592
8. Cheng, Y. S., Chen, C. C., Huang, C. H., Ko, T. P., Luo, W. H., Huang, J. W., Liu, J. R., and Guo, R. T. (2014) Structural analysis of a glycoside hydrolase family 11 xylanase from *Neocallimastix partriciarum*. *J. Biol. Chem.* **289**, 11020–11028
9. Xu, X., Liu, M. Q., Huo, W. K., and Dai, X. J. (2016) Obtaining a mutant of *Bacillus amyloliquefaciens* xylanase A with improved catalytic activity by directed evolution. *Enzyme Microb. Technol.* **86**, 59–66
10. Teng, C., Jiang, Y. F., Xu, Y. Q., Li, Q., Li, X. T., Fan, G. S., Xiong, K., Yang, R., Zhang, C. N., Ma, R., Zhu, Y. P., Li, J. L., and Wang, C. T. (2019) Improving the thermostability and catalytic efficiency of GH11 xylanase PjxA by adding disulfide bridges. *Int. J. Biol. Macromol.* **128**, 354–362
11. Wu, X. Y., Tian, Z. N., Jiang, X. K., Zhang, Q., and Wang, L. S. (2018) Enhancement in catalytic activity of *Aspergillus niger* XynB by selective site-directed mutagenesis of active site amino acids. *Appl. Microbiol. Biotechnol.* **102**, 249–260
12. Cheng, Y. S., Chen, C. C., Huang, J. W., Ko, T. P., Huang, Z. Y., and Guo, R. T. (2015) Improving the catalytic performance of a GH11 xylanase by rational protein engineering. *Appl. Microbiol. Biotechnol.* **99**, 9503–9510
13. Li, Q., Sun, B. G., Jia, H. Y., Hou, J., Yang, R., Xiong, K., Xu, Y. Q., and Li, X. T. (2017) Engineering a xylanase from *Streptomyce rochi* L10904 by mutation to improve its catalytic characteristics. *Int. J. Biol. Macromol.* **101**, 366–372
14. Chang, S. Y., Guo, Y. L., Wu, B., and He, B. F. (2017) Extracellular expression of alkali tolerant xylanase from *Bacillus subtilis* Lucky9 in *E. coli* and application for xylooligosaccharides production from agro-industrial waste. *Int. J. Biol. Macromol.* **96**, 249–256
15. Silva, S. B., Pinheiro, M. P., Fuzo, C. A., Silva, S. R., Ferreira, T. L., Lourenzoni, M. R., Nonato, M. C., Vieira, D. S., and Ward, R. J. (2017) The role of local residue environmental changes in thermostable mutants of the GH11 xylanase from *Bacillus subtilis*. *Int. J. Biol. Macromol.* **97**, 574–584
16. Ayadi, D. Z., Sayari, A. H., Hlima, H. B., Mabrouk, S. B., Mezghani, M., and Bejar, S. (2015) Improvement of *Trichoderma reesei* xylanase II thermal stability by serine to threonine surface mutations. *Int. J. Biol. Macromol.* **72**, 163–170
17. Wang, Q., Du, W., Weng, X. Y., Liu, M. Q., Wang, J. K., and Liu, J. X. (2015) Recombination of thermo-alkalistable, high xylooligosaccharides producing endo-xylanase from *Thermobifida fusca* and expression in *Pichia pastoris*. *Appl. Biochem. Biotechnol.* **175**, 1318–1329
18. Linares-Pasten, J. A., Aronsson, A., and Karlsson, E. N. (2018) Structural considerations on the use of endo-xylanases for the production of prebiotic xylooligosaccharides from biomass. *Curr. Protein Pept. Sci.* **19**, 48–67
19. Yin, X. J., Liu, Y. Y., Meng, L. J., Zhou, H. S., Wu, J. P., and Yang, L. R. (2020) Semi-rational hinge engineering: Modulating the conformational transformation of glutamate dehydrogenase for enhanced reductive amination activity towards non-natural substrates. *Catal. Sci. Technol.* **10**, 3376–3386
20. Wang, X. Y., Huang, H. Q., Xie, X. M., Ma, R., Bai, Y. G., Zheng, F., You, S., Zhang, B. Y., Xie, H. F., and Luo, H. Y. (2016) Improvement of the catalytic performance of a hyperthermostable GH10 xylanase from *Talaromyces leycettanus* JCM12802. *Bioresour. Technol.* **222**, 277–284
21. Yang, J. K., Ma, T. F., Shang-guan, F., and Han, Z. G. (2020) Improving the catalytic activity of thermostable xylanase from *Thermotoga maritima via* mutagenesis of non-catalytic residues at glycone subsites. *Enzyme Microb. Technol.* **139**, 109579

22. Vieira, D. S., and Ward, R. J. (2012) Conformation analysis of a surface loop that controls active site access in the GH11 xylanase A from *Bacillus subtilis*. *J. Mol. Model.* **18**, 1473–1479
23. Wu, X. Y., Zhang, S., Zhang, Q., Zhao, Y., Chen, G. J., Guo, W. H., and Wang, L. S. (2020) The contribution of specific subsites to catalytic activities in active site architecture of a GH11 xylanase. *Appl. Microbiol. Biotechnol.* **104**, 8735–8745
24. Alponti, J. S., Maldonado, R. F., and Ward, R. J. (2016) Thermostability of *Bacillus subtilis* GH11 xylanase by surface charge engineering. *Int. J. Biol. Macromol.* **87**, 522–528
25. Tian, L., Liu, S., Wang, S., and Wang, L. (2016) Ligand-binding specificity and promiscuity of the main lignocellulolytic enzyme families as revealed by active-site architecture analysis. *Sci. Rep.* **6**, 23605
26. Damis, S. I. R., Murad, A. M. A., Bakar, F. D. A., Rashid, S. A., Jaafar, N. R., and Illias, R. M. (2019) Protein engineering of GH11 xylanase from *Aspergillus fumigatus* RT-1 for catalytic efficiency improvement on kenaf biomass hydrolysis. *Enzyme Microb. Technol.* **131**, 109383
27. Pollet, A., Lagaert, S., Eneyskaya, E., Kulminskaya, A., Delcour, J. A., and Courtin, C. M. (2010) Mutagenesis and subsite mapping underpin the importance for substrate specificity of the aglycon subsites of glycoside hydrolase family 11 xylanases. *Biochim. Biophys. Acta* **1804**, 977–985
28. Li, X. Q., Wu, Q., Hu, D., Wang, R., Liu, Y., Wu, M. C., and Li, J. F. (2017) Improving the temperature characteristics and catalytic efficiency of a mesophilic xylanase from *Aspergillus oryzae*, AoXyn11A, by iterative mutagenesis based on in silico design. *AMB Express* **9**, 97
29. Wang, G. Z., Wu, J. J., Lin, J., Ye, X. Y., and Yao, B. (2016) The disruption of two salt bridges of the cold-active xylanase XynGR40 results in an increase in activity, but a decrease in thermostability. *Biochem. Biophys. Res. Commun.* **481**, 139–145
30. Han, N. Y., Ma, Y., Mu, Y. L., Tang, X. H., Li, J. J., and Huang, Z. X. (2019) Enhancing thermal tolerance of a fungal GH11 xylanase guided by B-factor analysis and multiple sequence alignment. *Enzyme Microb. Technol.* **131**, 109422
31. Han, N. Y., Miao, H. B., Ding, J. M., Li, J. J., Mu, Y. L., Zhou, J. P., and Huang, Z. X. (2017) Improving the thermostability of a fungal GH11 xylanase *via* site-directed mutagenesis guided by sequence and structural analysis. *Biotechnol. Biofuels* **10**, 138
32. Vucinic, J., Novikov, G., Montanier, C. Y., Dumon, C., and Schiex, T. (2021) A comparative study to decipher the structural and dynamics determinants underlying the activity and thermal stability of GH11 xylanases. *Int. J. Mol. Sci.* **22**, 5961
33. Leys, S., Pauly, A., Delcour, J. A., and Courtin, C. M. (2016) Modification of the secondary binding site of xylanases illustrates the impact of substrate selectivity on bread making. *J. Agric. Food Chem.* **64**, 5400–5409
34. Torronen, A., and Rouvinen, J. (1995) Structural comparison of two major endo-1,4-xylanase from *Trichoderma reesei*. *Biochemistry* **34**, 847–856
35. Lammerts Van Bueren, A., Otani, S., Friis, E. P., Wilson, K. S., and Davies, G. J. (2012) Three-dimensional structure of a thermophilic family GH11 xylanase from *Thermobifida fusca*. *Acta Crystallogr. Sect. F Struct. Biol. Cryst. Commun.* **68**, 141
36. Murakami, M. T., Ruller, R., Ward, R. J., and Arni, R. K. (2005) Crystal structure of a mesophilic xylanase A from *Bacillus subtilis* 1A1. *FEBS Lett.* **579**, 6505–6510
37. Wan, Q., Zhang, Q., Hamilton-Brehm, S., Weiss, K., Mustyakimov, M., Coates, L., Langan, P., Graham, D., and Kovalevsky, A. (2014) X-ray crystallographic studies of family 11 xylanase Michaelis and product complexes: Implications for the catalytic mechanism. *Acta Crystallogr. D Biol. Crystallogr.* **70**, 11–23
38. Bradford, M. M. (1976) A rapid and sensitive method for the quantitation of microgram quantities of protein utilizing the principle of protein-dye binding. *Anal. Biochem.* **72**, 248–254
39. Fonseca-Maldonado, R., Vieira, D. S., Alponti, J. S., Bonneil, E., Thibault, P., and Ward, R. J. (2013) Engineering the pattern of protein glycosylation modulates the thermostability of a GH11 xylanase. *J. Biol. Chem.* **288**, 25522–25534
40. Abraham, M. J., Murtola, T., Schulz, R., Pall, S., Smith, J. C., Hess, B., and Lindahl, E. (2015) Gromacs: High performance molecular simulations through multi-level parallelism from laptops to supercomputers. *SoftwareX* **1-2**, 19–25
41. Wu, B., Yu, Q., Chang, S. Y., Pedroso, M. M., Gao, Z., He, B. F., and Schenk, G. (2019) Expansin assisted bio-affinity immobilization of endoxylanase from *Bacillus subtilis* onto corncob residue: Characterization and efficient production of xylooligosaccharides. *Food Chem.* **282**, 101–108